

Silicon Photonics Layout Report

[RS_0925]

September 2025

1 Introduction

This report summarizes the layout I created after three weeks of learning the “**Silicon Photonics Design, Fabrication and Data Analysis**” course offered on edX by the University of British Columbia (UBC). I found the course to be intensive but highly engaging and enjoyable. The structured lectures and hands-on assignments provided an excellent foundation for understanding silicon photonics, layout design, and simulation workflows.

In this report, I present a brief overview of the layout design that I created as part of the course project, including the waveguide and Mach-Zehnder Interferometer (MZI) structures implemented in KLayout using the EBeam PDK. The layout incorporates a set of straight waveguides of different lengths for propagation loss characterization and multiple MZI configurations for investigating the effects of coupler type, path length difference, and waveguide bends on optical transmission and free spectral range (FSR).

The report further includes simulation results for all these structures, followed by a Monte Carlo statistical analysis to study fabrication-induced variability. Together, these results demonstrate the complete workflow from design to simulation that I learned through the course, emphasizing both the theoretical understanding and the practical implementation of silicon photonic devices.

2 Layout Description

The layout was implemented using KLayout and is shown in Figure 1. The design fits within an area constraint of $410\text{ }\mu\text{m} \times 605\text{ }\mu\text{m}$, following the guidelines required for compatibility with automated measurement setups at UBC’s silicon photonics laboratory.

2.1 Waveguide Test Structures

At the bottom-left corner, four straight waveguides were designed with Bragg grating couplers at both ends. Figure 2 inside the box (dotted cyan) show these structures.

The lengths of the waveguides are:

- $200\text{ }\mu\text{m}$ (cell: WG200)
- $400\text{ }\mu\text{m}$ (cell: WG400)
- $600\text{ }\mu\text{m}$ (cell: WG600)
- $800\text{ }\mu\text{m}$ (cell: WG800)

These test structures will be used to measure the propagation loss per cm of the waveguides. By comparing the transmission through each waveguide, the incremental loss as a function of length can be extracted.

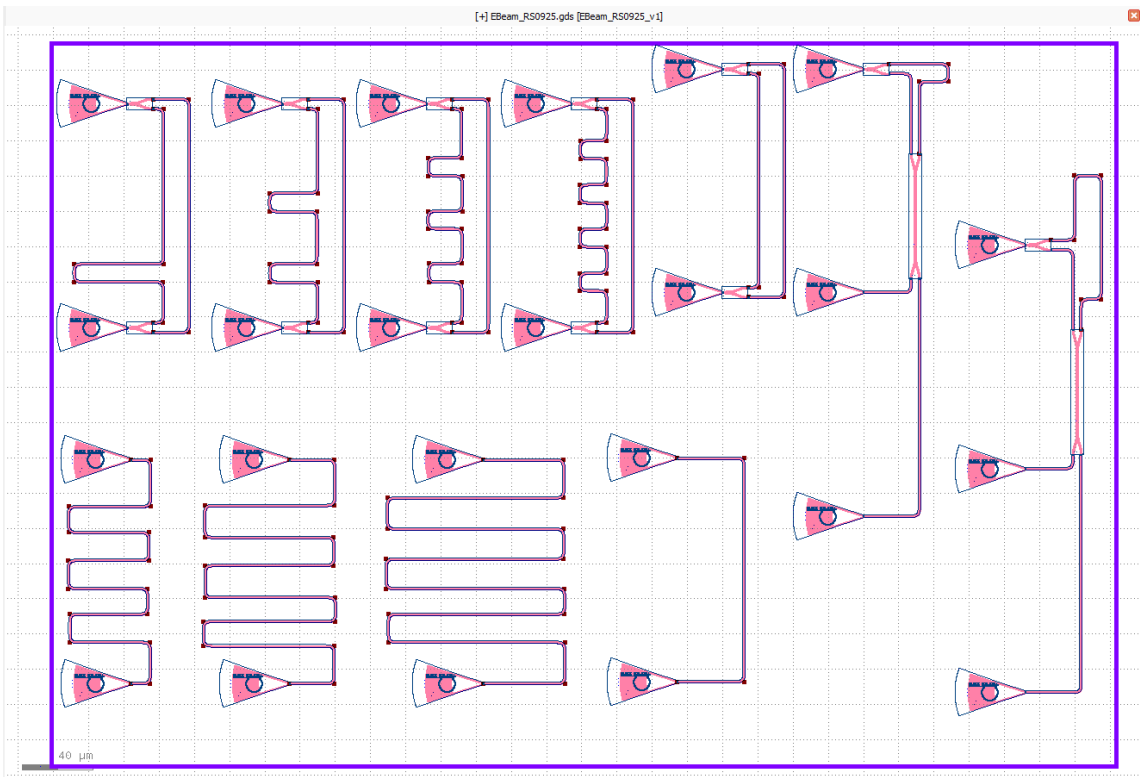


Figure 1: KLayout design created after 3 weeks of the UBC edX Silicon Photonics course.

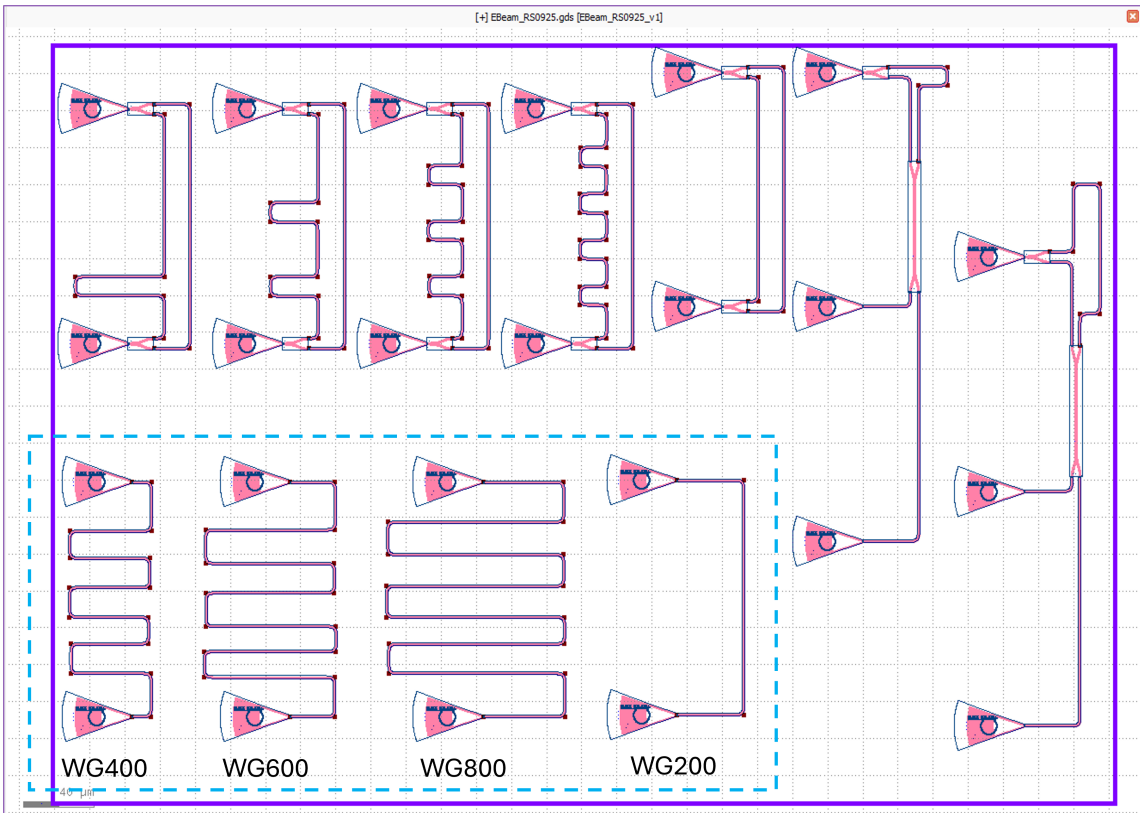


Figure 2: KLayout design: Basic waveguide structures with variable lengths.

2.2 Mach-Zehnder Interferometers (MZIs) – Top Right

Three MZI modulators were designed in the top-right corner (figure 3):

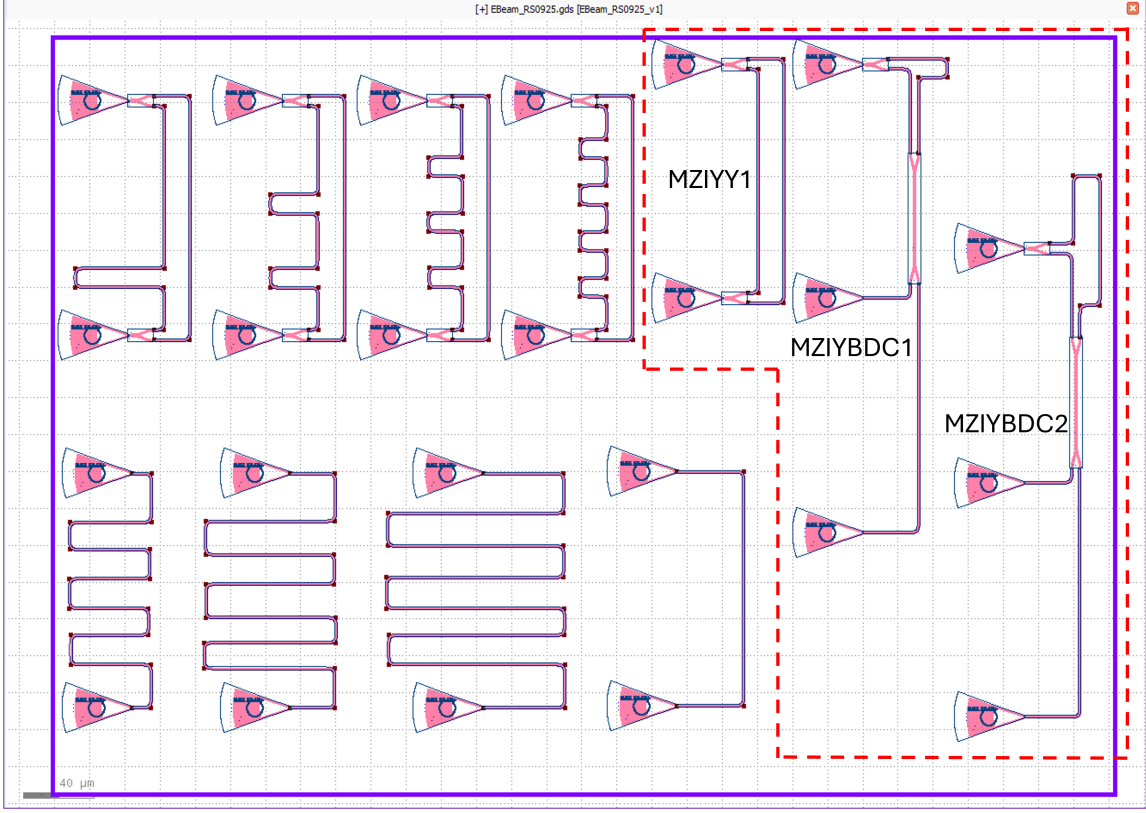


Figure 3: KLayout design: Mach-Zehnder Interferometers (MZIs) with different coupling components and different path difference.

1. **First MZI (cell - MZIYY1):** A Y-splitter at the input followed by two arms with a path length difference of $40 \mu\text{m}$, recombined using a Y-combiner.
2. **Second MZI (cell - MZIYBDC1):** Similar path length difference ($39.883 \mu\text{m}$), but recombination is performed with a broadband directional coupler instead of a Y-combiner.
3. **Third MZI (cell - MZIYBDC2):** Similar structure to the second, but with a larger path difference of $100 \mu\text{m}$. This will help study how the free spectral range (FSR) and insertion gain vary as the path difference increases.

Device ID	Upper Arm (WG1)	Lower Arm (WG2)	Path Difference (ΔL)
MZIYY1	$130.001 \mu\text{m}$	$170.001 \mu\text{m}$	$40.000 \mu\text{m}$
MZIYBDC1	$56.118 \mu\text{m}$	$96.001 \mu\text{m}$	$39.883 \mu\text{m}$
MZIYBDC2	$55.968 \mu\text{m}$	$156.000 \mu\text{m}$	$100.032 \mu\text{m}$

Table 1: Waveguide arm lengths and path length differences for MZI Set 1 (Top-Right MZIs).

The purpose of this set of structures (Figure 3, table 2) is to evaluate the effect of different combining mechanisms (Y-combiner vs. directional coupler) and path length differences on the modulation performance, gain, and FSR.

2.3 Mach-Zehnder Interferometers (MZIs) – Top Left

Four additional MZI structures (cells: MZIYY20, MZIYY21, MZIYY22 and MZIYY23) were designed at the top-left corner. In these:

- The right-hand arm remains fixed in shape and length.
- The left-hand arm maintains the same length as the right arm but varies in shape (different bending configurations).

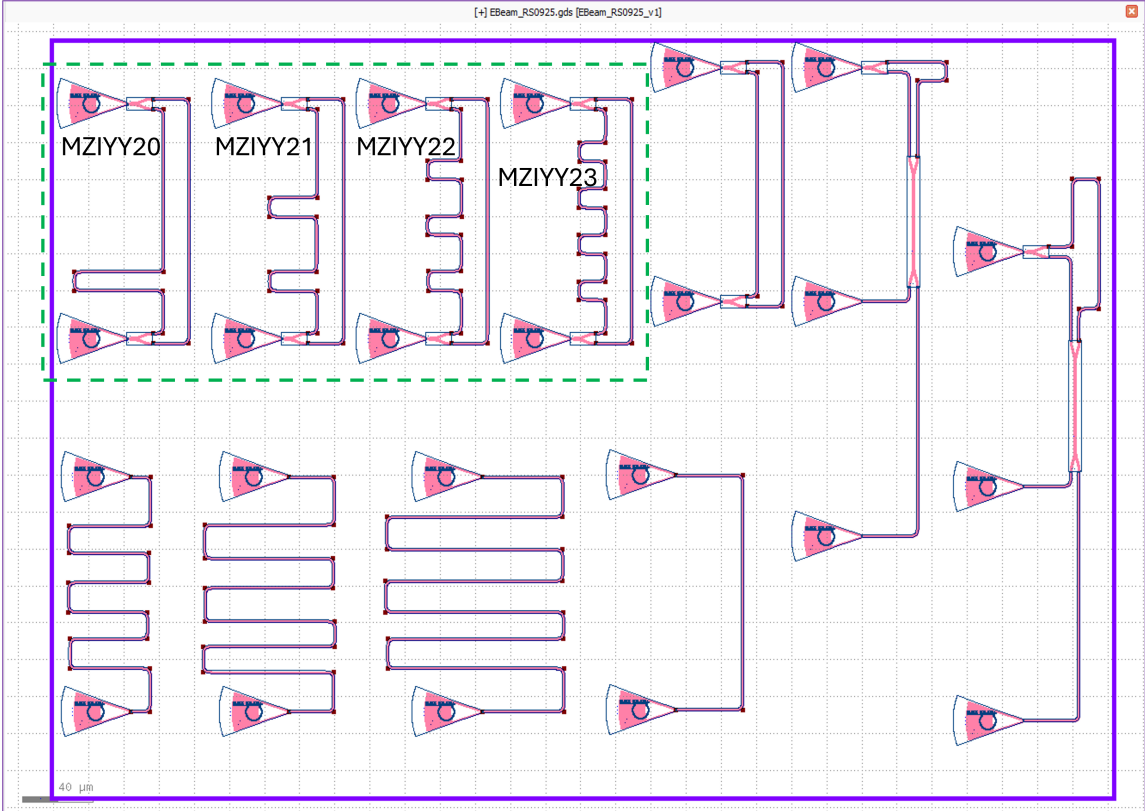


Figure 4: KLayout design: MZI structures with same path difference and variable number of bends.

Device ID	Upper Arm (wg1)	Lower Arm (wg2)	Path Difference (ΔL)
MZIYY20	225.000 μm	170.001 μm	54.999 μm
MZIYY21	225.010 μm	170.001 μm	55.009 μm
MZIYY22	224.999 μm	170.001 μm	54.998 μm
MZIYY23	224.990 μm	170.001 μm	54.989 μm

Table 2: Waveguide arm lengths and path length differences for MZI Set 2 (Top-Left MZIs).

These structures (Figure 4, table 2) will allow an experimental investigation of bend-induced losses and their impact on device performance. Simulations indicated negligible impact, but fabrication and measurement will confirm whether bend losses can be quantified with this configuration.

3 Design Considerations

The layout was constrained within the $410 \mu\text{m} \times 605 \mu\text{m}$ area while maintaining compatibility with automated test setups. Careful consideration was given to waveguide tapering, coupler placement, and routing in order to minimize footprint while still enabling accurate characterization.

4 Simulation Results: Waveguides

The waveguide structures were simulated to extract the wavelength-dependent transmission and loss. Each waveguide was defined as a separate cell: WG200, WG400, WG600, and WG800. The simulated n_{eff} and n_g for these waveguides (width = 500 nm, height = 220 nm) is found to be 2.4450516 and 4.19896, respectively, at $\lambda_0 = 1550$ nm.

4.1 Single Waveguide (WG200)

Figure 5 shows the gain vs. wavelength for the 200 μm waveguide (WG200). The gain spectrum peaks around 1550 nm with an insertion loss of approximately -5 dB.

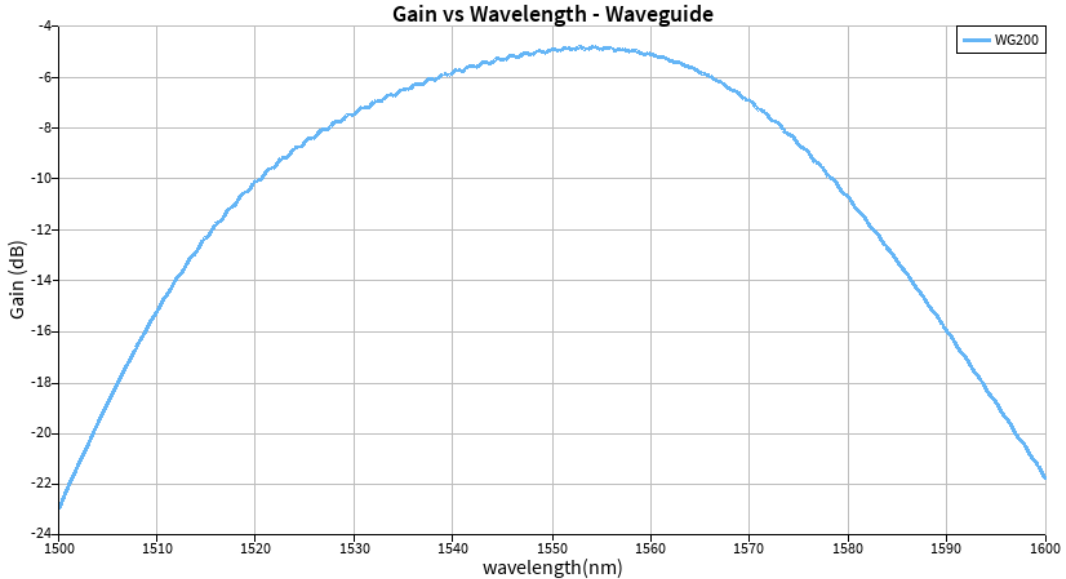


Figure 5: Gain vs. wavelength for WG200 (200 μm waveguide).

4.2 Comparison of Different Lengths

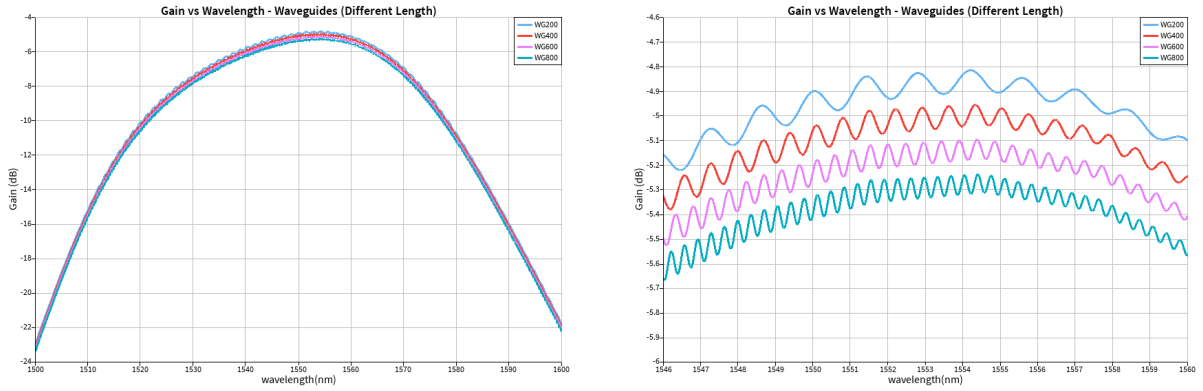
Figures 6 shows the gain spectra of waveguides with different lengths. The periodic oscillations arise due to Fabry-Perot effects between the grating couplers.

4.3 Loss Estimation

From the transmission spectra, the relative insertion losses between WG200, WG400, WG600, and WG800 can be compared. By plotting transmission vs. length at a fixed wavelength (e.g., 1550 nm), the slope provides an estimate of the propagation loss in dB/cm. This analysis will be performed in future experimental measurements after fabrication.

5 Simulation Results: MZIs (Top-Right Set)

The first set of Mach-Zehnder Interferometers (MZIs) corresponds to the top-right corner of the layout. These include three cells: **MZIYY1**, **MZIYBDC1**, and **MZIYBDC2**. Here, “Y” refers to a Y-splitter/combiner, and “BDC” indicates a broadband directional coupler. The main goal of this study is to evaluate the impact of different combining mechanisms and path differences on the gain, phase shift, and free spectral range (FSR).



(a) Gain vs. wavelength for WG200, WG400, WG600, and WG800 across the full 1500–1600 nm range.

(b) Zoomed-in gain vs. wavelength around 1546–1560 nm for different waveguide lengths.

Figure 6: Gain vs. wavelength for the Waveguides of variable lengths.

5.1 Transmission Gain

Figure 7 shows the transmission spectrum of **MZIYY1**, which employs Y-splitters at both input and output. The envelope of the spectrum also reflects the characteristic response of the Bragg grating couplers used in the layout.

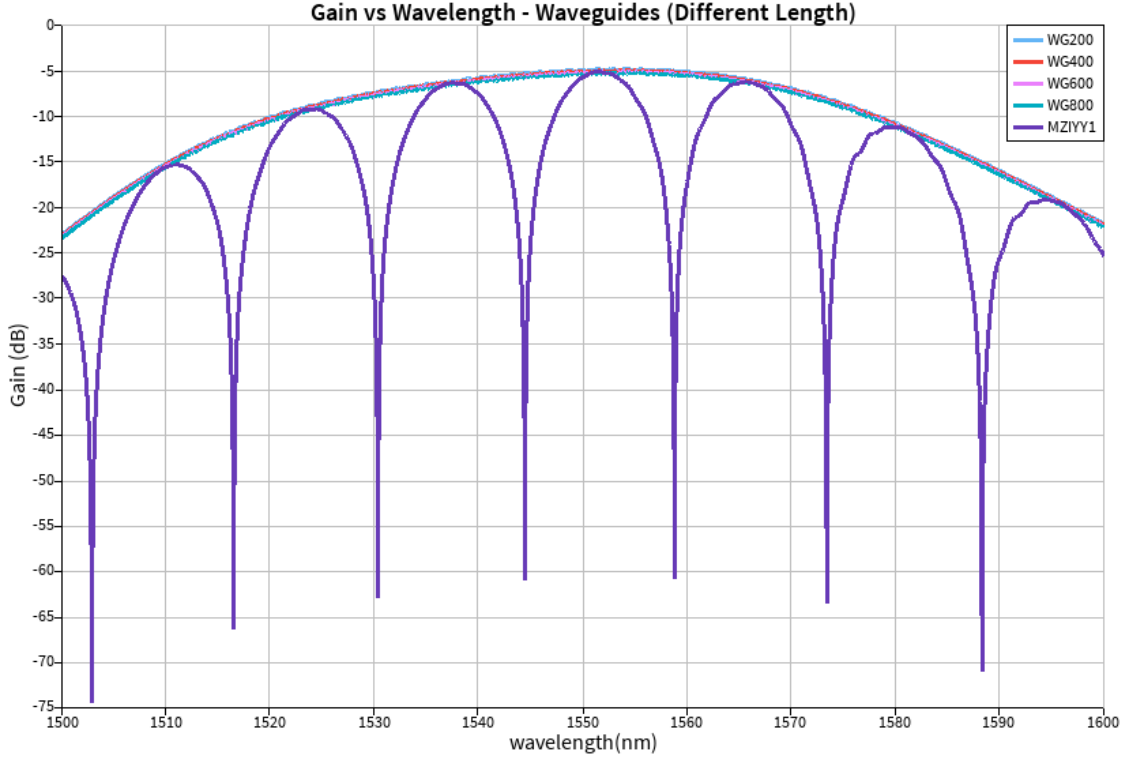


Figure 7: Transmission gain vs. wavelength for MZIYY1. The shape is strongly influenced by the Bragg grating coupler response.

The next two structures employ broadband directional couplers (BDCs) for recombination. Figures 8 and 9 show the transmission spectra at both ports of **MZIYBDC1** and **MZIYBDC2**, respectively. As expected, the outputs are orthogonal in nature, confirming correct power splitting behavior.

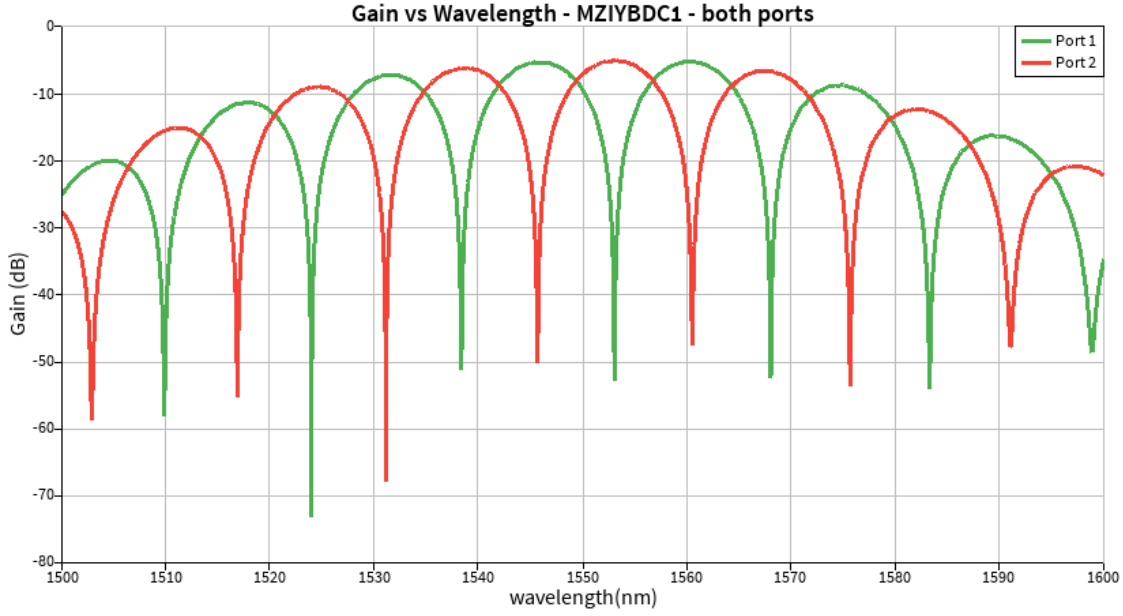


Figure 8: Transmission gain vs. wavelength for MZIYBDC1 (ports 1 and 2). Orthogonal outputs are observed.

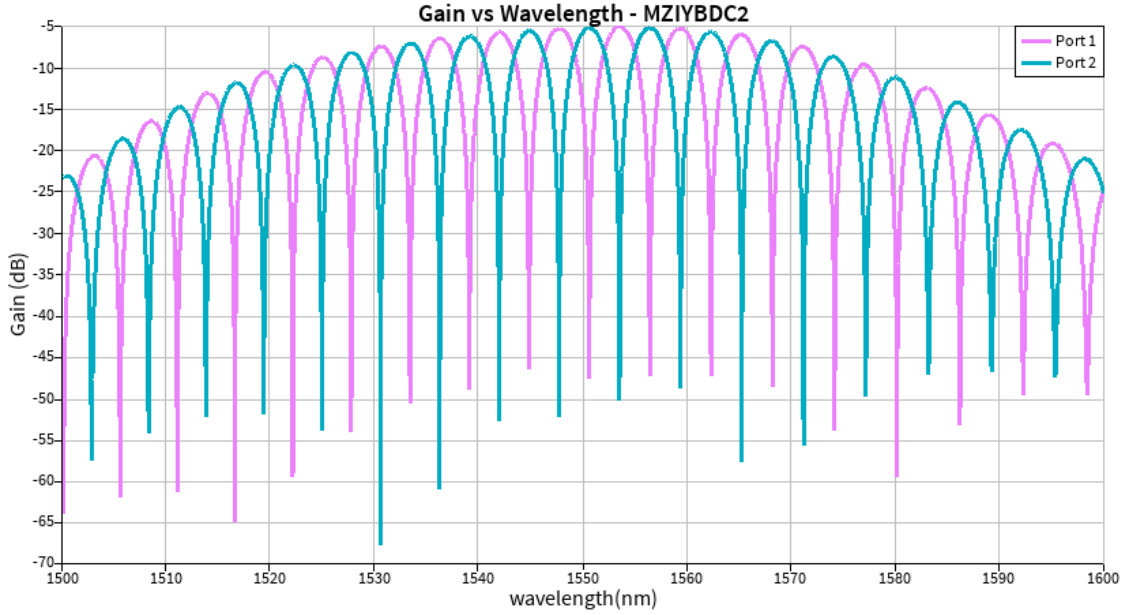


Figure 9: Transmission gain vs. wavelength for MZIYBDC2 (ports 1 and 2). Orthogonal outputs are observed.

5.2 Comparison of All MZIs

To compare the effects of different combining schemes and path differences, the gain responses of all three MZIs are plotted together in Figure 10. This comparison highlights the phase shift behavior and the variation in FSR among the devices.

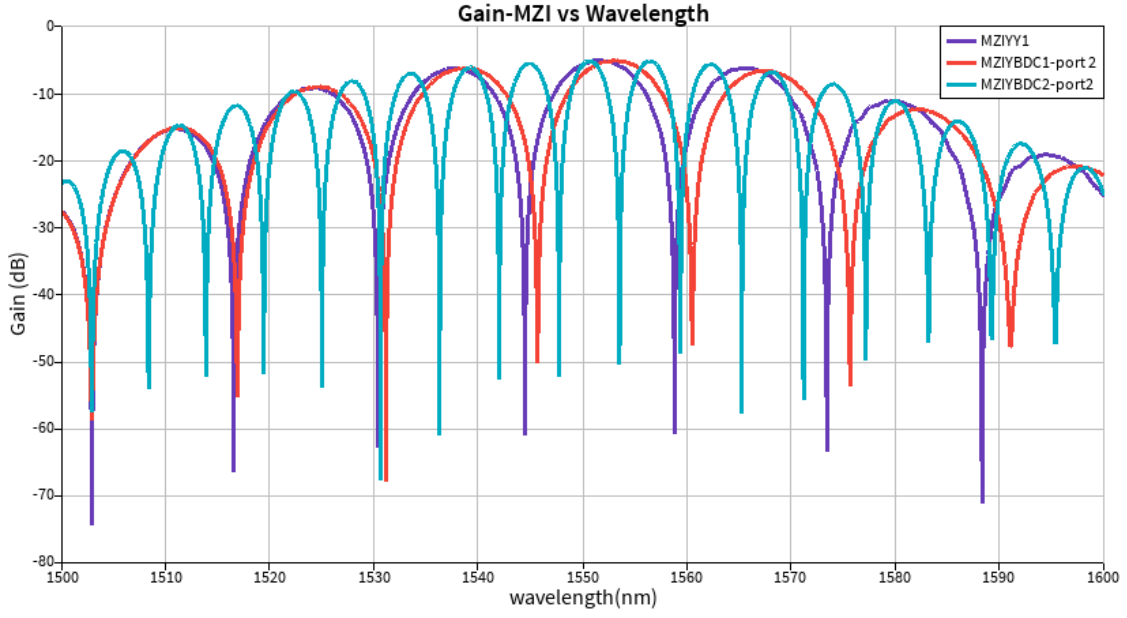


Figure 10: Comparison of gain vs. wavelength for all three MZIs (MZIYY1, MZIYBDC1, and MZIYBDC2).

5.3 Free Spectral Range (FSR) Analysis

The simulated FSR values for all three MZI structures are shown in Figure 11. As expected, the device with the larger path length difference (MZIYBDC2) exhibits a smaller FSR (refer the theoretical calculated values in table 3). The plots confirm that device geometry and combiner type both play a role in spectral performance.

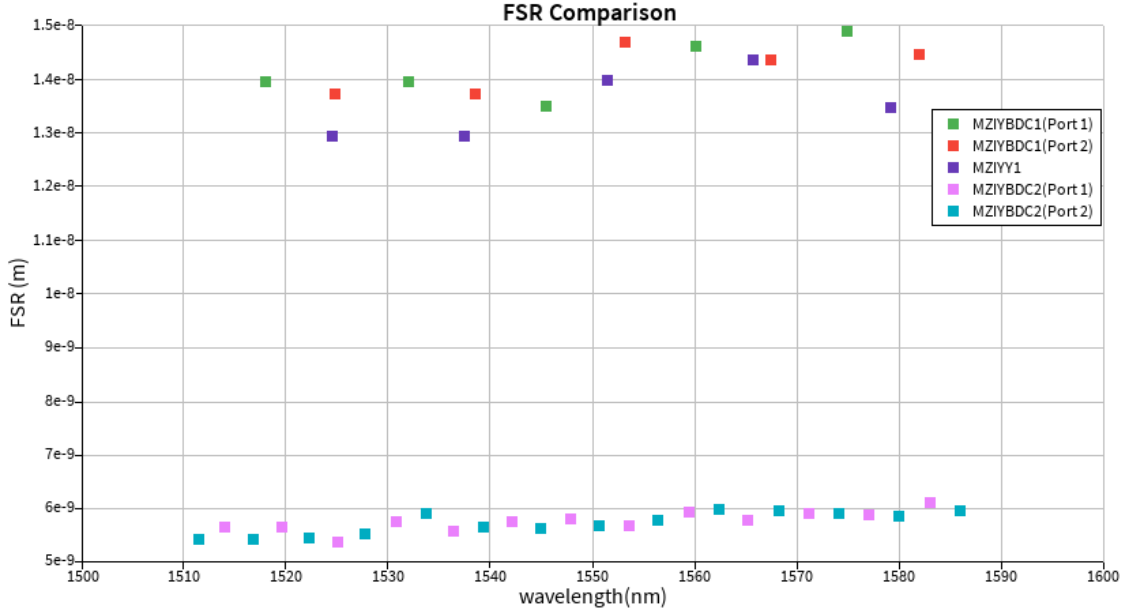


Figure 11: Simulated FSR comparison of the three MZIs. Larger path differences lead to smaller FSR values.

Device ID	ΔL (μm)	FSR @ 1550 nm (nm)
MZIYY1	40.000	14.304
MZIYBDC1	39.883	14.346
MZIYBDC2	100.032	5.720

Table 3: Calculated FSRs for MZI Set 1 using $n_g = 4.19896$ and $\lambda_0 = 1550 \text{ nm}$.

6 Simulation Results: MZIs (Top-Left Set)

The second set of Mach-Zehnder Interferometers (MZIs) corresponds to the top-left corner of the layout (cells: **MZIYY20**, **MZIYY21**, **MZIYY22**, and **MZIYY23**). In these designs, the right-hand arm is kept fixed in both length and shape, while the left-hand arm is modified to include different bend configurations. All devices maintain the same total length difference, thus isolating the effect of bends on performance. The bends were designed with a radius of $5 \mu\text{m}$, optimized using the Bézier coefficient available in the EBeam PDK.

6.1 Gain Comparison

The gain spectra of the four MZIs are compared in Figure 12. As expected, the transmission responses overlap almost completely, confirming that the bend-induced loss at this radius is negligible in simulation.

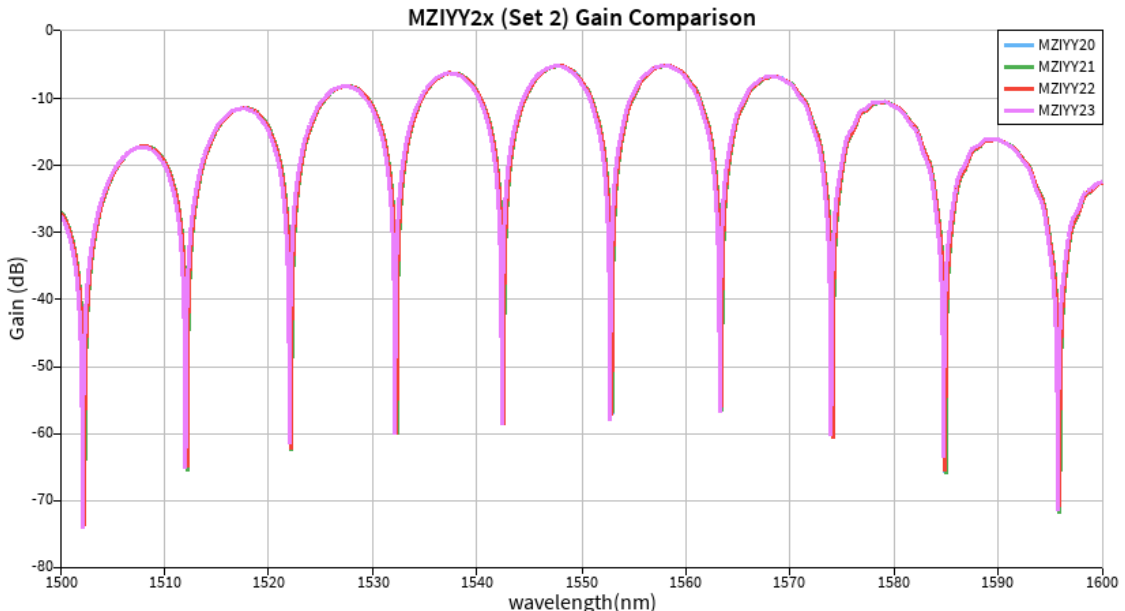


Figure 12: Gain vs. wavelength for the second set of MZIs (MZIYY20–MZIYY23). Negligible difference is observed, confirming minimal bend loss.

6.2 FSR Analysis

The FSR values of the four structures are shown in Figure 13. The curves remain very close to each other (refer the theoretical calculated values in table 4), again indicating that the bends do not significantly impact the device free spectral range. The small variations observed are within expected simulation tolerances.

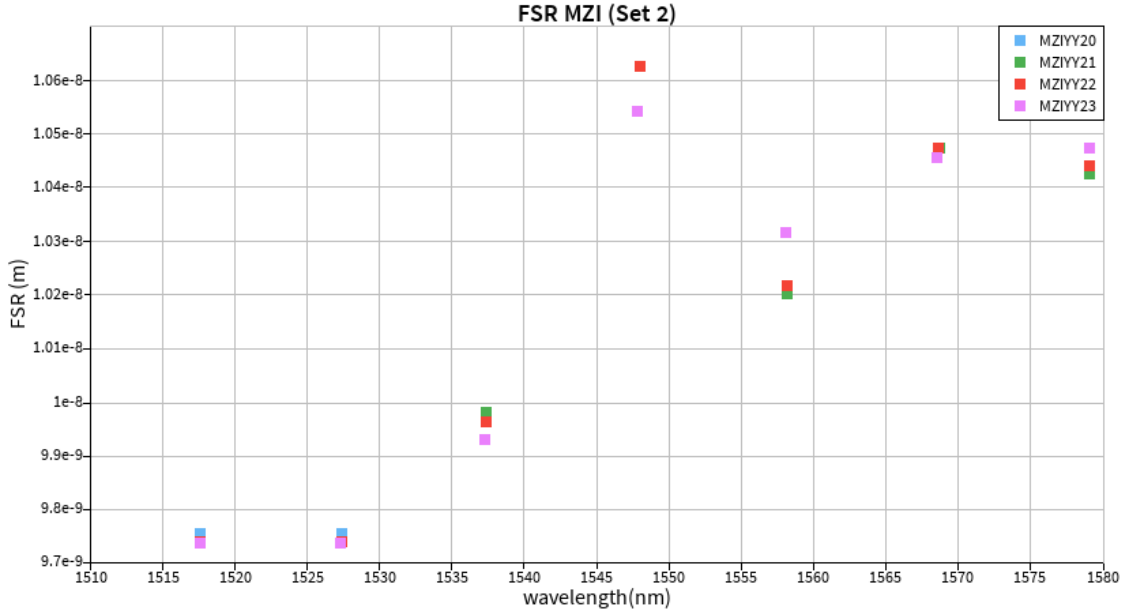


Figure 13: Simulated FSR comparison of the second MZI set (MZIYY20–MZIYY23). Results show negligible impact from waveguide bends.

Device ID	ΔL (μm)	FSR @ 1550 nm (nm)
MZIYY20	54.999	10.403
MZIYY21	55.009	10.401
MZIYY22	54.998	10.403
MZIYY23	54.989	10.405

Table 4: Calculated FSRs for MZI Set 2 using $n_g = 4.19896$ and $\lambda_0 = 1550 \text{ nm}$.

6.3 Discussion

The results confirm that bends with a radius of $5 \mu\text{m}$ (optimized with the Bézier coefficient) do not introduce measurable additional loss in simulation. However, fabrication-induced imperfections such as sidewall roughness, etch non-uniformities, and lithography resolution limits may introduce additional scattering losses. It will therefore be important to validate these findings experimentally once fabricated devices are available.

7 Comparison of MZI Sets

To consolidate the findings, Table 5 compares the key characteristics of the two MZI sets. Set 1 focuses on the effect of different combining mechanisms (Y vs. BDC) and path length differences, while Set 2 evaluates the impact of bends in otherwise identical arm lengths.

8 Monte Carlo Simulation Results

To evaluate the sensitivity of the designed devices to fabrication variability, Monte Carlo simulations were carried out using the EBeam PDK framework. Both *on-wafer* (intra-wafer) random variations and *wafer-to-wafer* systematic shifts were included. The analysis was performed for the straight waveguide (WG200) and the interferometric device (MZIYY1).

MZI Set	Device IDs	Design Variation and Key Observations
Set 1 (Top-Right)	MZIYY1, MZIYBDC1, MZIYBDC2	Y vs. BDC combiner; path differences of 40 μm and 100 μm . Spectral responses strongly influenced by path difference. BDC structures show orthogonal outputs. Larger path difference \rightarrow smaller FSR.
Set 2 (Top-Left)	MZIYY20, MZIYY21, MZIYY22, MZIYY23	Different bend shapes with fixed path length. Minimal difference in gain and FSR. Bend loss negligible with 5 μm radius (Bézier optimized). Fabrication effects may still introduce measurable loss.

Table 5: Summary comparison of the two MZI sets in the layout.

8.1 Monte Carlo Parameters and Variation Model

Figure 14 shows the parameter windows used in the simulations. Two categories of variation were modeled:

- **On-wafer (intra-wafer) variation:** Random local fluctuations across a single die/wafer, representing critical dimension (CD) variation, sidewall roughness, and local etch non-uniformity. Each device instance on the wafer is perturbed independently.
- **Wafer-to-wafer variation:** Global shifts applied to all devices on a given wafer, representing systematic drifts in lithography, resist, or etch processes. These variations have a correlation length across the wafer, modeling slow drifts on the millimeter scale.

Variation Type	Parameter	Std. Dev. / Correlation
On-wafer (intra-wafer)	Width variation	$\sigma = 5 \text{ nm}$
	Thickness variation	$\sigma = 3 \text{ nm}$
Wafer-to-wafer	Width variation	$\sigma = 5 \text{ nm}$, corr. length $= 4.5 \times 10^{-3} \text{ m}$
	Height variation	$\sigma = 2 \text{ nm}$, corr. length $= 4.5 \times 10^{-3} \text{ m}$

Table 6: Monte Carlo simulation variation parameters for waveguide and MZI devices.

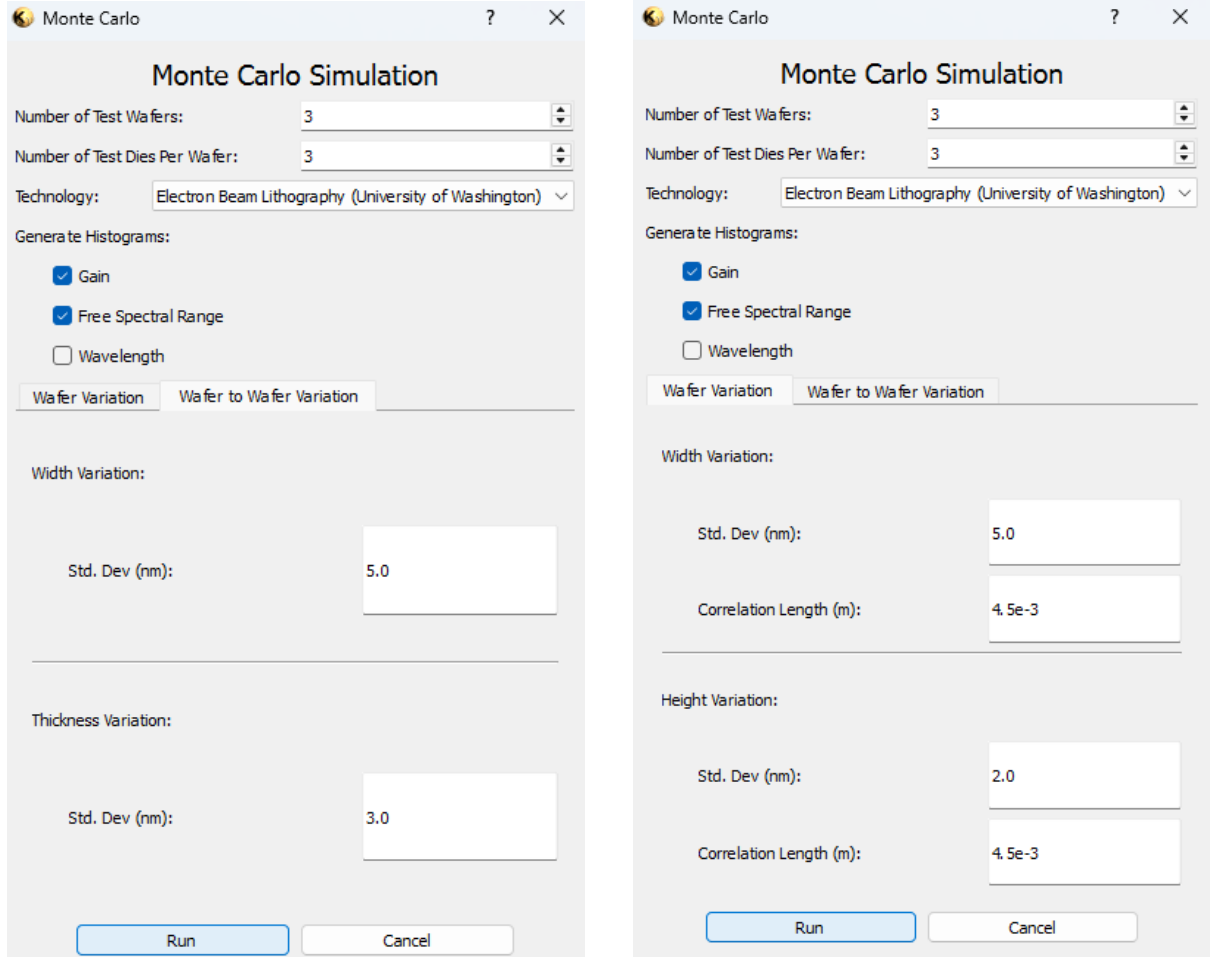
8.2 WG200 Monte Carlo Analysis

Monte Carlo analysis of the 200 μm waveguide was performed across 3 wafers and 3 dies per wafer. Fig. 15 presents the transmission spectra for multiple runs, while the resulting gain distribution is shown in Fig. 16.

The results show that the straight waveguide is relatively robust, with only small shifts in insertion loss and bandwidth under fabrication variability.

8.3 MZIYY1 Monte Carlo Analysis

Monte Carlo simulations for the interferometric device MZIYY1 reveal higher sensitivity to dimensional drifts. The gain spectra for nine runs are shown in Fig. 17. Histograms of peak



(a) On-wafer (intra-wafer) variation settings.

(b) Wafer-to-wafer variation settings.

Figure 14: Monte Carlo simulation parameter windows used in the EBeam PDK flow.

gain and free spectral range (FSR) are provided in Figs. 18 and 19.

8.4 Discussion

The Monte Carlo study highlights the different sensitivities of straight and interferometric devices:

- **WG200:** Low sensitivity to variability, with gain variations limited to ± 1 dB.
- **MZIYY1:** Much stronger sensitivity, with peak gain standard deviation of ~ 4.5 dB, reflecting the critical dependence of interferometers on path length and refractive index control.
- **FSR stability:** The FSR distribution is narrower (mean ~ 13.7 nm, std. dev ~ 0.5 nm), showing that path difference remains relatively stable under the modeled variations.

These results emphasize that while waveguides are robust against fabrication noise, interferometric devices require tighter dimensional control or active trimming/compensation techniques to ensure stable performance.

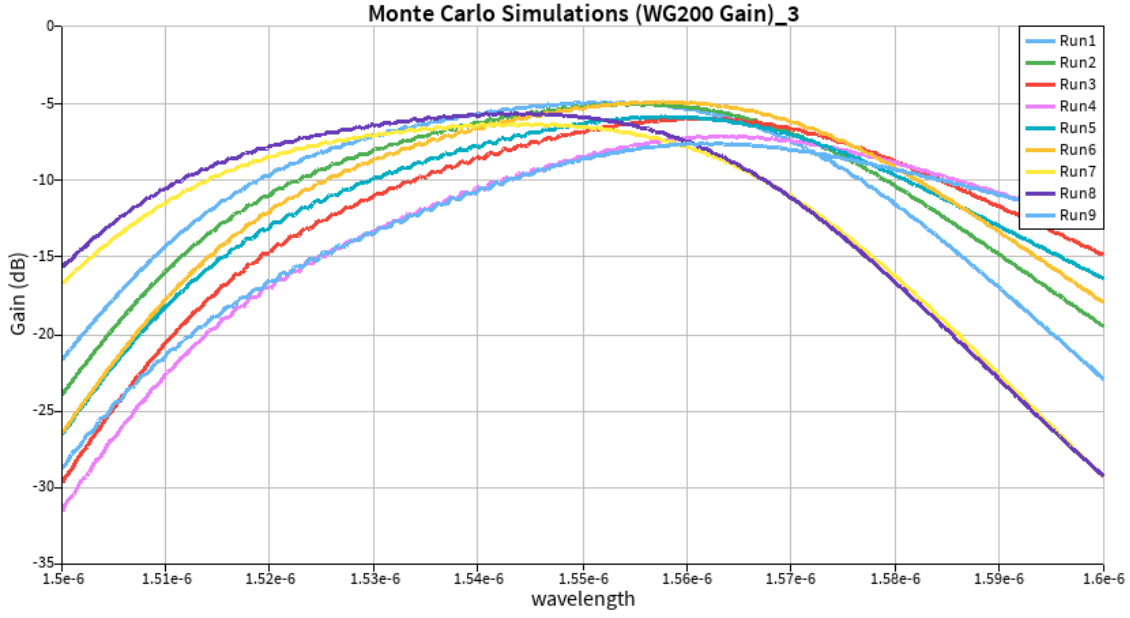


Figure 15: Monte Carlo transmission spectra for WG200 over nine simulation runs. Fabrication variability shifts the gain and bandwidth slightly.

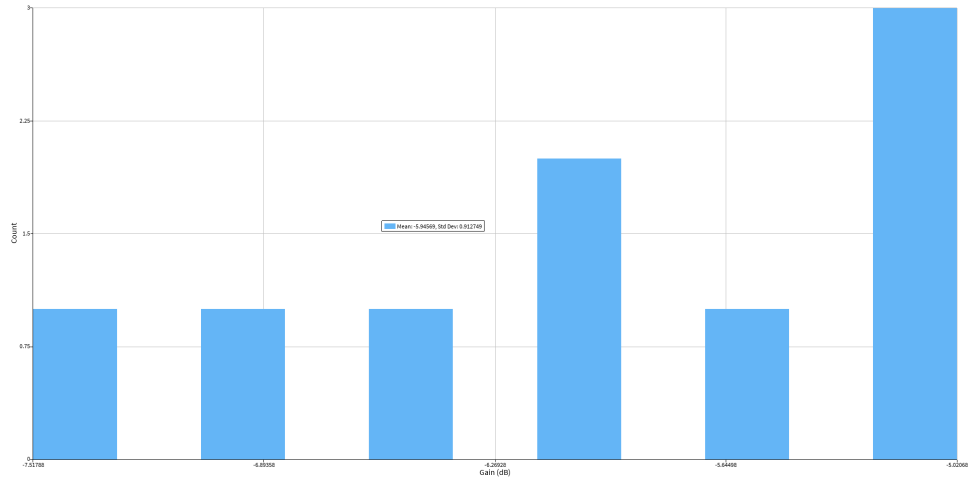


Figure 16: Histogram of WG200 gain variation (mean: -5.95 dB, std. dev: 0.91 dB).

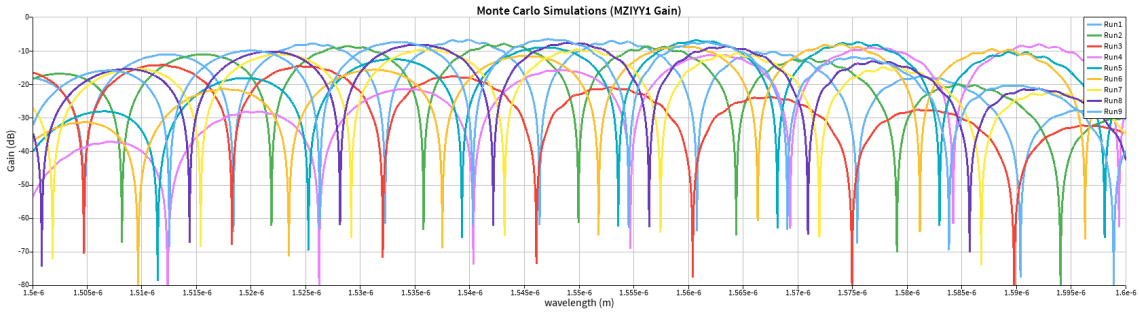


Figure 17: Monte Carlo gain spectra for MZIYY1 over nine simulation runs. Strong variability is observed in transmission due to dimensional sensitivity.

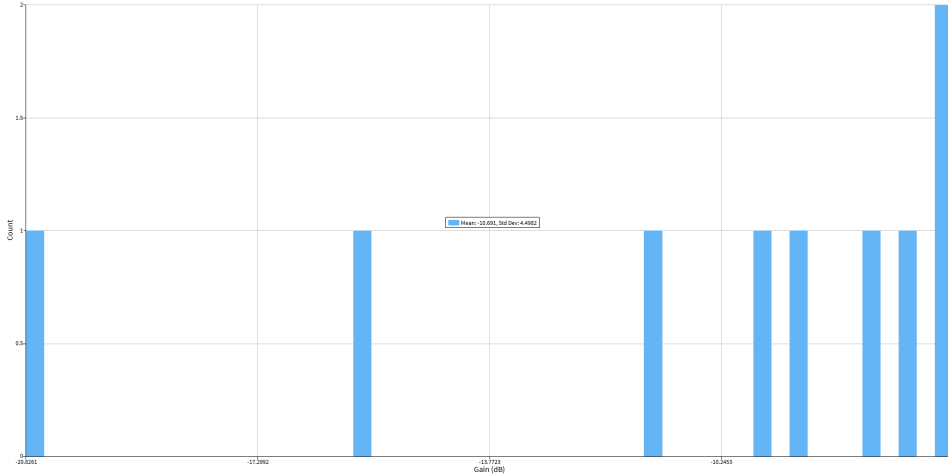


Figure 18: Histogram of MZIYY1 peak gain variation (mean: -10.7 dB, std. dev: 4.5 dB).

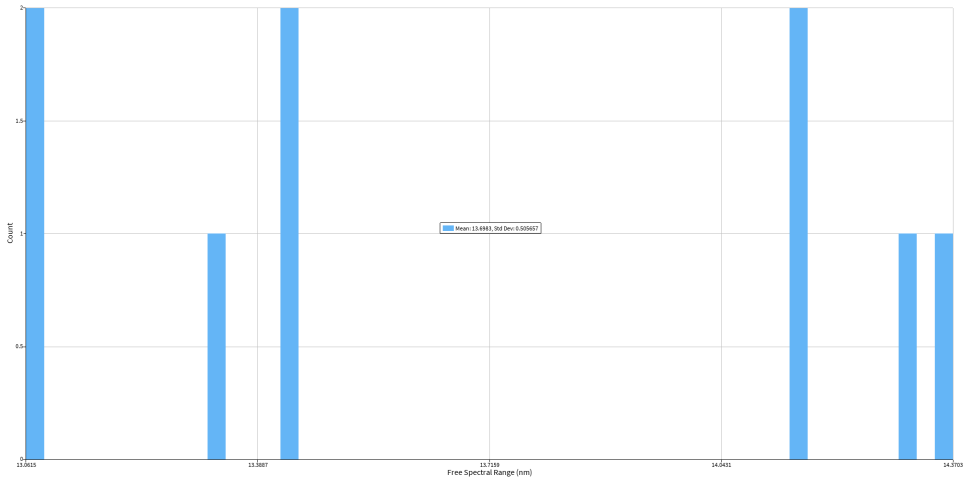


Figure 19: Histogram of MZIYY1 free spectral range (FSR) variation (mean: 13.7 nm, std. dev: 0.5 nm).

9 Waveguide Corner Analysis and Compact Modelling

To relate the fabricated devices to realistic process variations, a corner analysis was performed using Lumerical MODE. The silicon waveguide cross-section (nominal thickness $t_{\text{nom}} = 220$ nm, width $W_{\text{nom}} = 500$ nm) was simulated for three thickness values and three width values:

$$t = t_{\text{nom}} + \Delta t, \quad \Delta t \in \{0, +3.1 \text{ nm}, -4.7 \text{ nm}\},$$

$$W = W_{\text{nom}} + \Delta W, \quad \Delta W \in \{0, +10 \text{ nm}, -30 \text{ nm}\}.$$

This produces a 3×3 grid of cases, labelled according to the compact notation used in the course:

- **tw_n-n:** nominal thickness, nominal width,
- **tw_tmx-wmx:** maximum thickness, maximum width,
- **tw_tmn-wmn:** minimum thickness, minimum width,
- and similarly for the other edge and corner combinations.

For each case the fundamental mode was simulated, and the effective index $n_{\text{eff}}(\lambda)$ was fitted around $\lambda_0 = 1550$ nm using a second-order Taylor expansion

$$n_{\text{eff}}(\lambda) \approx n_1 + n_2(\lambda - \lambda_0) + n_3(\lambda - \lambda_0)^2.$$

From the fit coefficients, the group index and dispersion were obtained as

$$n_g = n_1 - \lambda_0 n_2, \quad D = -\frac{\lambda_0}{c} 2n_3.$$

Figure ?? (to be inserted) shows the 2D corner space (thickness vs. width) for both TE and TM modes. The numerical values for the fundamental TE and TM modes are summarized in Tables 7 and 8.

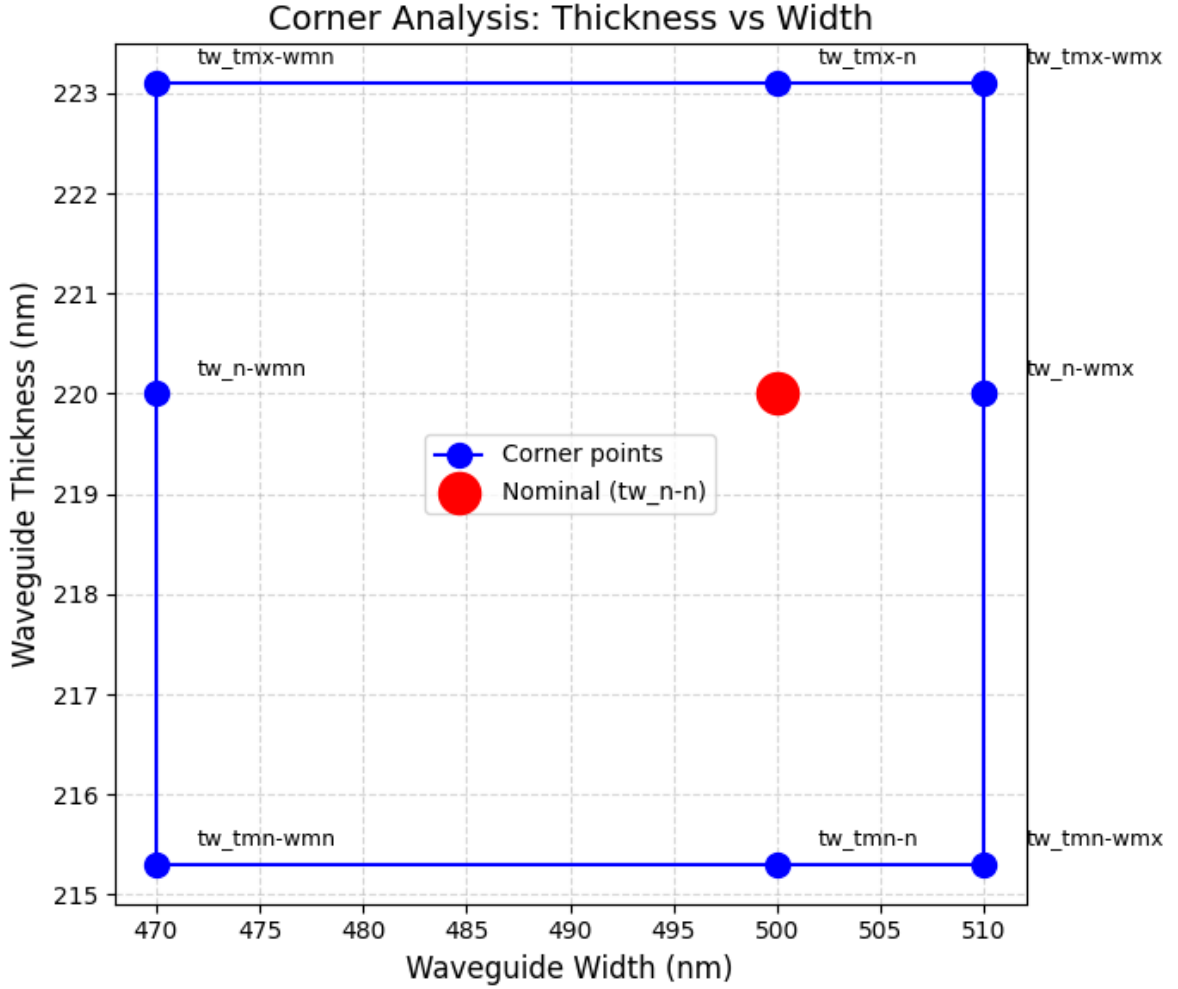


Figure 20: TE mode corner points.

TE-mode corner table

Across the TE corners, the group index spans approximately

$$n_g^{\text{TE}} \in [4.16, 4.24],$$

which sets a realistic process window for the devices that are designed and operated in TE polarization.

Case	t (nm)	W (nm)	n_{eff}	$n_{g,\text{fit}}$	D (ps/nm·km)
tw_n-n	220.0	500	2.4404	4.1771	3.18E-10
tw_n-wmx	220.0	510	2.4537	4.1604	3.13E-10
tw_n-wmn	220.0	470	2.3861	4.2311	2.55E-10
tw_tmx-n	223.1	500	2.4565	4.1886	4.01E-10
C1_tw_tmx-wmx	223.1	510	2.4699	4.1712	3.84E-10
C4_tw_tmx-wmn	223.1	470	2.4024	4.2427	3.57E-10
tw_tmn-n	215.3	500	2.4230	4.1732	2.18E-10
C2_tw_tmn-wmx	215.3	510	2.4365	4.1564	2.17E-10
C3_tw_tmn-wmn	215.3	470	2.3686	4.2261	1.22E-10

Table 7: Corner analysis for the fundamental TE mode: effective index, fitted group index, and dispersion at 1550 nm.

TM-mode corner table

Case	t (nm)	W (nm)	n_{eff}	$n_{g,\text{fit}}$	D (ps/nm·km)
tw_n-n	220.0	500	1.7746	3.7380	-1.88E-08
tw_n-wmx	220.0	510	1.7811	3.7599	-1.86E-08
tw_n-wmn	220.0	470	1.7525	3.6667	-1.94E-08
tw_tmx-n	223.1	500	1.7879	3.7987	-1.85E-08
C1_tw_tmx-wmx	223.1	510	1.7951	3.8191	-1.83E-08
C4_tw_tmx-wmn	223.1	470	1.7659	3.7293	-1.92E-08
tw_tmn-n	215.3	500	1.7371	3.5519	-1.89E-08
C2_tw_tmn-wmx	215.3	510	1.7436	3.5750	-1.87E-08
C3_tw_tmn-wmn	215.3	470	1.7168	3.4767	-1.93E-08

Table 8: Corner analysis for the fundamental TM mode: effective index, fitted group index, and dispersion at 1550 nm.

For the TM mode, the group index spans roughly

$$n_g^{\text{TM}} \in [3.48, 3.82],$$

which is relevant for TM-polarized components such as the on-chip laser structures used in separate experiments. In the rest of this report, the MZI devices are operated in TE polarization, and therefore the TE corner envelope in Table 7 is the main reference for comparing with measurements.

10 Measurements and Data Analysis

10.1 Waveguide Loss Measurement

In this part of the experiment, four straight waveguides: WG200, WG400, WG600 and WG800 with different lengths (200, 400, 600, and 800 μm respectively) were measured in order to estimate the waveguide propagation loss. Each waveguide includes its own pair of grating couplers for fiber-to-chip coupling. The measured transmission therefore contains both the grating coupler loss and the waveguide loss.

The transmission spectra of all four waveguides were first smoothed using a Savitzky–Golay filter (refer fig.21). This was done to reduce the Fabry -Pérot ripples and noise in the raw data so that the general trend of the measurements becomes easier to analyze. After smoothing, the transmission values at 1550 nm were taken for each waveguide length.

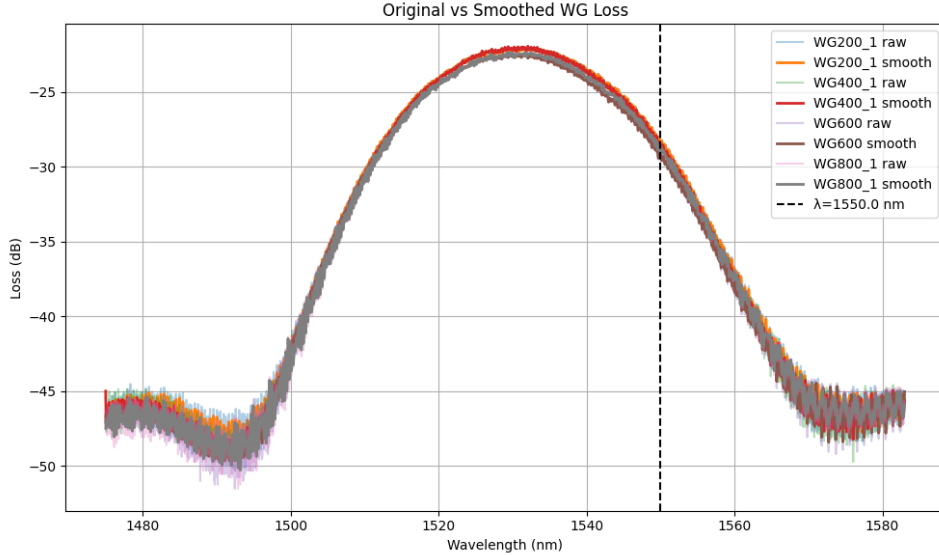


Figure 21: Measured Waveguide structure losses and smoothened data.

The idea was to apply the cut-back method, where the transmission is plotted as a function of waveguide length. If the grating coupler loss is the same for all devices, the slope of this line gives the propagation loss in dB/cm. However, in our case the results did not show a clear linear trend. The measured losses for the four waveguides were all very close to each other (only about 0.6 dB difference, refer table 9), and the linear fit produced a low R^2 value (around 0.5). This means the data does not follow a straight line very well.

Table 9: Smoothed transmission values at 1550 nm for the four waveguides.

Waveguide	Length (cm)	Loss at 1550 nm (dB)
WG200	0.02	-28.492
WG400	0.04	-28.565
WG600	0.06	-29.061
WG800	0.08	-28.798

This happens mainly because each waveguide uses a different pair of grating couplers. Small differences in grating coupler performance from device to device are larger than the small amount of loss caused by the extra waveguide length (only a few hundred micrometers). As a result, the cut-back method cannot be applied reliably with these structures.

Although we cannot extract an accurate propagation loss, the small variation in transmission among the four waveguides suggests that the actual waveguide loss is relatively low, likely a few dB/cm. The grating coupler loss extracted from the data is about 14 dB per coupler, which is within a reasonable range for non-optimized designs.

For a proper cut-back measurement, much longer waveguides are required. Typically, waveguides with lengths of several centimeters (for example, 2 to 10 cm) are used so that the propagation loss dominates over any variations in grating coupler efficiency. Such structures would make it possible to obtain a reliable and accurate value for the waveguide loss.

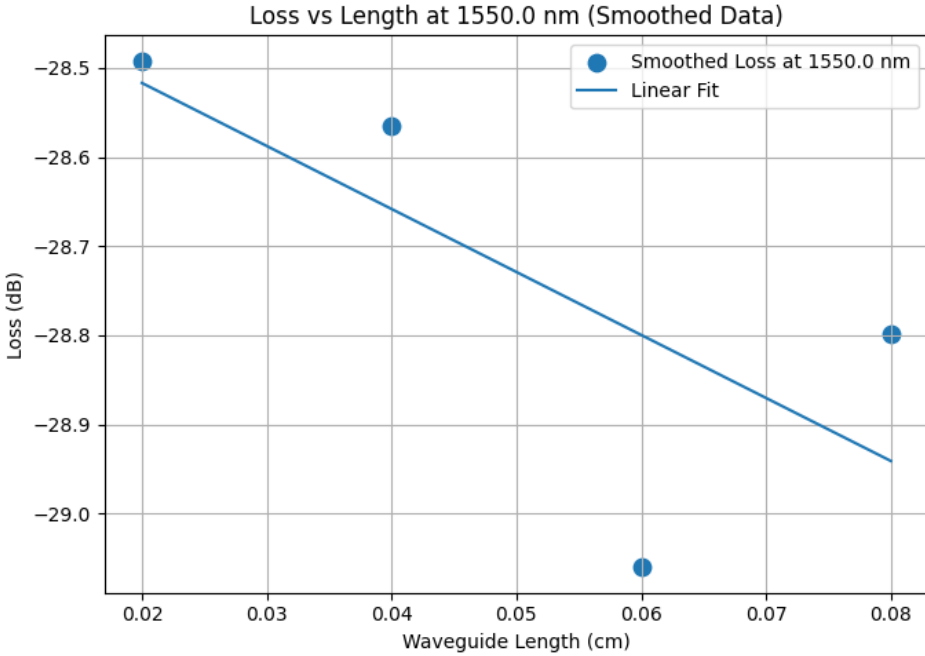


Figure 22: Measured Waveguide structure losses and smoothened data.

10.2 Measured Characterization of Set-2 MZIs (MZIYY20–MZIYY23)

The second set of Mach–Zehnder interferometers (MZIYY20–MZIYY23) was designed with nearly identical optical path-length differences and different bend geometries in one of the arms. The goal of this set is to verify, experimentally, whether the optimized bends (radius 5 μm with Bézier shaping in the EBeam PDK) introduce any measurable change in the free-spectral range (FSR) or group index, beyond what is expected from process variations captured by the corner analysis.

Raw Measured Transmission and Initial Peak Detection

Transmission spectra were measured from approximately 1470 nm to 1600 nm using the automated measurement setup. An example of the raw spectrum for device MZIYY20 is shown in Fig. 23. The interference fringes are clearly visible, but the trace also contains noise and residual spectral ripple from the grating couplers.

A straightforward peak-finding algorithm applied directly to this raw trace leads to over-detection, because local noise maxima are falsely identified as resonant peaks. This is illustrated in Fig. 24, where the red crosses show detected peaks without any pre-processing.

Savitzky–Golay Smoothing and Robust Peak Extraction

To obtain reliable peak positions, the measured spectra were processed in Python using a multi-stage pipeline:

1. Application of a Savitzky–Golay filter (polynomial order 3 with an appropriate window size) to smooth high-frequency noise while preserving the overall fringe shape.
2. Derivative-based peak detection on the smoothed trace.
3. Peak filtering based on minimum prominence and minimum spacing to eliminate spurious detections.

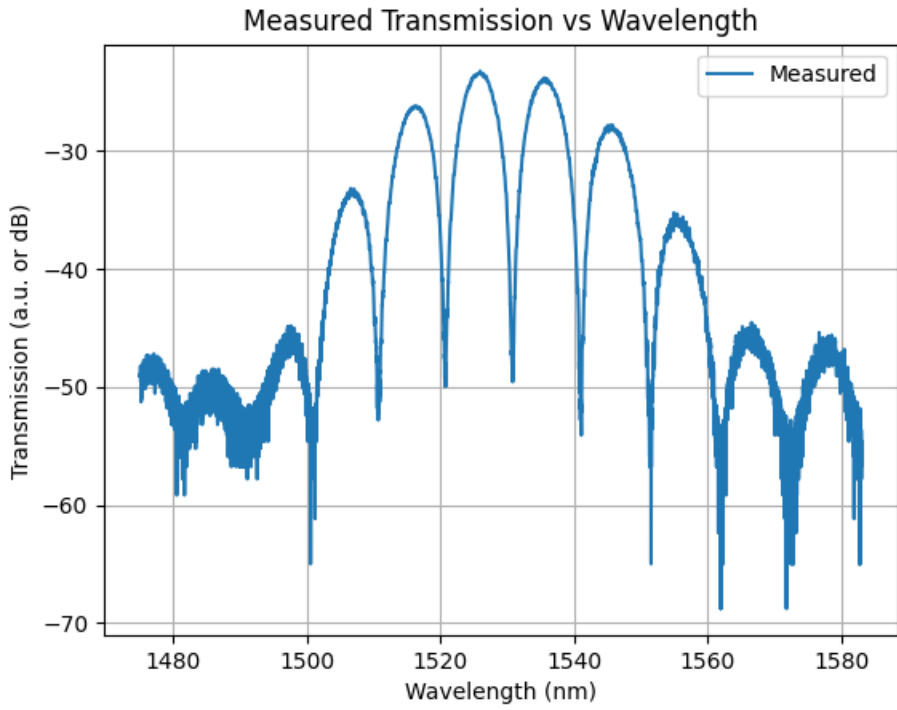


Figure 23: Raw measured transmission spectrum for MZIYY20.

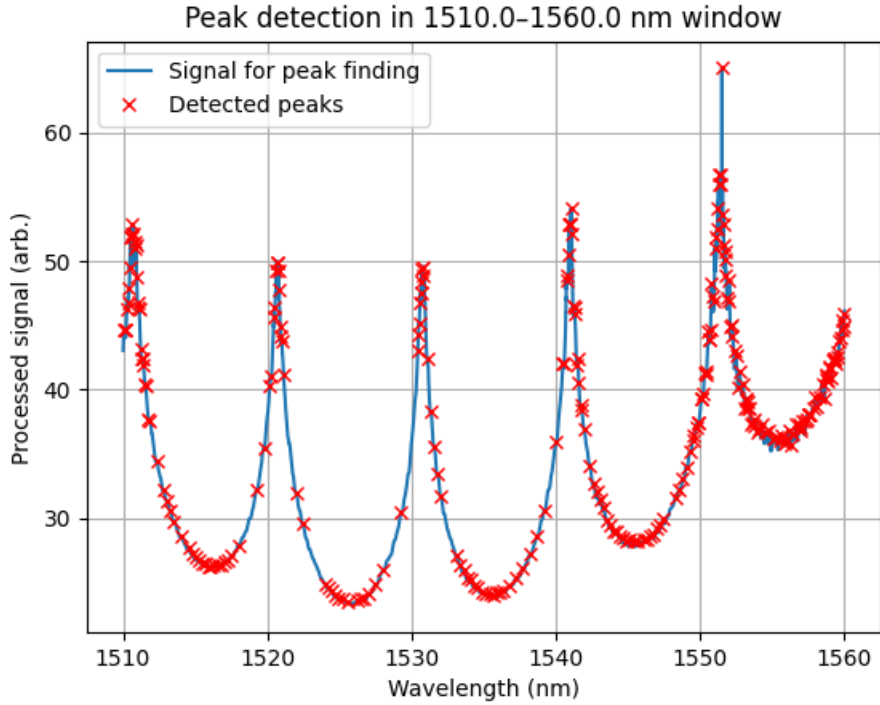


Figure 24: Naïve peak detection on the raw MZIYY20 data: noisy and unreliable peak locations.

Figure 25 shows an example of peak detection in a smaller wavelength window after this processing. The blue curve is the processed signal used for peak finding and the red markers represent the cleaned set of detected peaks. The overall smoothed spectrum for MZIYY20 is

shown in Fig. 26.

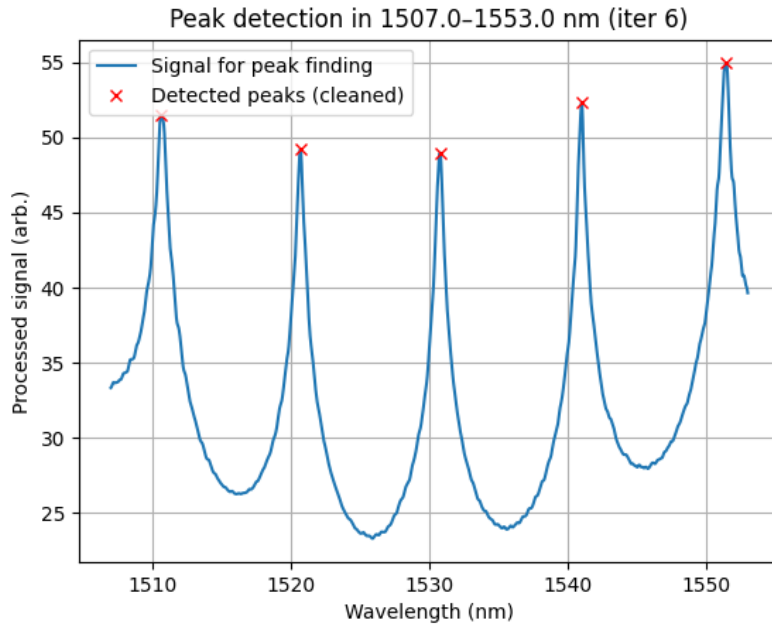


Figure 25: Peak detection on the smoothed MZIYY20 spectrum in a narrower wavelength window.

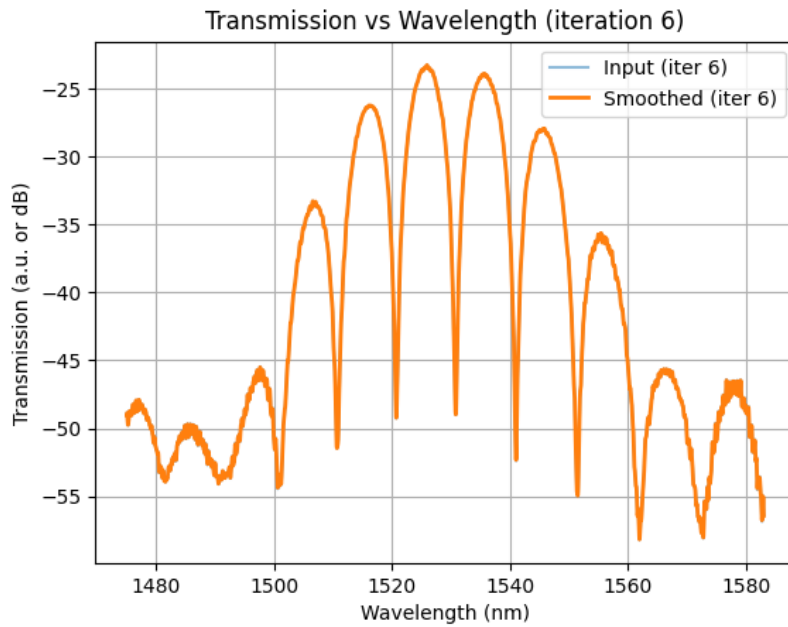


Figure 26: Smoothed transmission spectrum for MZIYY20 after Savitzky–Golay filtering.

These processing steps significantly improve the robustness of peak detection and therefore of the FSR extraction, compared with directly analysing the raw data.

De-embedding Using the WG200_1 Reference Waveguide

To isolate the intrinsic MZI response from the contribution of the grating couplers and common routing, a de-embedding procedure was performed using the reference straight waveguide device WG200_1 (length 200 μm) present on the same die. The de-embedding was carried out as follows:

1. Convert both MZI and WG200_1 transmission spectra to linear scale.
2. Form the ratio $T_{\text{MZI}}/T_{\text{WG200_1}}$ within a 10 dB window around the maximum of WG200_1 to avoid amplifying noise outside the usable range.
3. Convert back to dB units to obtain the de-embedded loss spectrum of each MZI.

The resulting de-embedded spectra for MZIYY20–MZIYY23 are plotted in Fig. 27. The fringe shapes and depths are very similar across all four devices, confirming that bend-induced excess loss is negligible and that the primary differences arise from small effective-index variations.

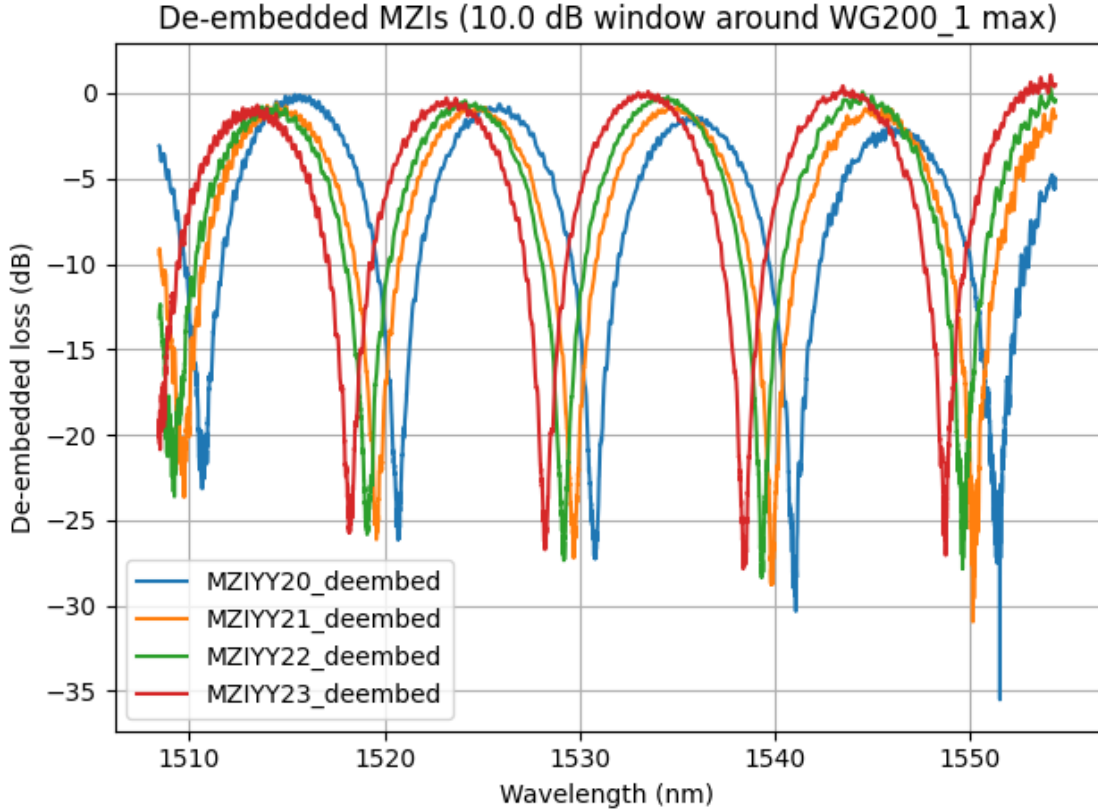


Figure 27: De-embedded loss spectra for MZIYY20–MZIYY23 using WG200_1 as the reference waveguide.

Simulated and Measured FSR and Group Index

Using the cleaned peak positions from the smoothed and de-embedded data, the measured free-spectral range FSR_{meas} was determined from the spacing between successive maxima ($\lambda_{k+1} - \lambda_k$). The corresponding measured group index $n_{g,\text{meas}}$ was calculated using

$$\text{FSR} = \frac{\lambda_0^2}{n_g \Delta L},$$

where $\lambda_0 \approx 1550$ nm and ΔL is the optical path-length difference between the MZI arms.

Simulated FSR values FSR_{sim} were obtained using the group index from MODE simulations and the same relation, with the nominal design values of ΔL .

Table 10 summarizes the simulated and measured performance of the four Set-2 MZIs.

Device	ΔL (μm)	FSR_{sim} (nm)	$n_{g,\text{sim}}$	FSR_{meas} (nm)	$n_{g,\text{meas}}$
MZIYY20	$225 - 170.001 \approx 54.999$	10.6094	4.11733	10.4400	4.18408
MZIYY21	$225.001 - 170.001 \approx 55.000$	10.6094	4.11726	10.3520	4.21965
MZIYY22	$224.999 - 170.001 \approx 54.998$	10.6587	4.09839	10.2880	4.24605
MZIYY23	$224.990 - 170.001 \approx 54.989$	10.5083	4.15773	10.2720	4.25336

Table 10: Simulated and measured FSR and group index for Set-2 MZIs (MZIYY20–MZIYY23).

Discussion

The measured FSR values for MZIYY20–MZIYY23 are consistently slightly lower than their simulated counterparts, corresponding to slightly higher measured group indices. This behaviour is consistent with the corner-analysis results presented earlier, where realistic process variations in waveguide thickness and width led to n_g values in the range of approximately 4.16–4.24. The experimentally extracted values for these four MZIs (4.18–4.25) fall within this range, validating both the waveguide compact model and the corner-analysis methodology.

Furthermore, the strong similarity between the de-embedded spectra of all four devices indicates that the different bend layouts used in MZIYY20–MZIYY23 do not introduce significant additional loss or dispersion at the chosen bend radius. The observed device-to-device differences are therefore dominated by fabrication-induced variations rather than by the bend geometry itself.

10.3 Measured Characterization of Set-1 MZIs (MZIYY1_1, MZIBDC1, MZIBDC2)

The first set of Mach–Zehnder interferometers consists of three devices that differ in their arm-length differences and in the combining mechanism (Y-combiner vs. broadband directional coupler). This set is primarily intended to evaluate the influence of coupler architecture and path-length difference on the free-spectral range (FSR) and extracted group index.

- **MZIYY1_1:** Y-splitter and Y-combiner, $\Delta L = 40 \mu\text{m}$
- **MZIBDC1:** Y-splitter and broadband directional coupler (BDC), $\Delta L \approx 39.883 \mu\text{m}$
- **MZIBDC2:** Y-splitter and BDC, $\Delta L \approx 100.032 \mu\text{m}$

Raw Measured Data and Processing Pipeline

As with Set 2, the raw measured spectra exhibit a high level of noise and residual grating-coupler ripple. An example raw spectrum is shown in Fig. 28. These fluctuations make direct peak detection difficult, as shown in Fig. 29, where noisy local maxima are mistakenly identified as interference peaks.

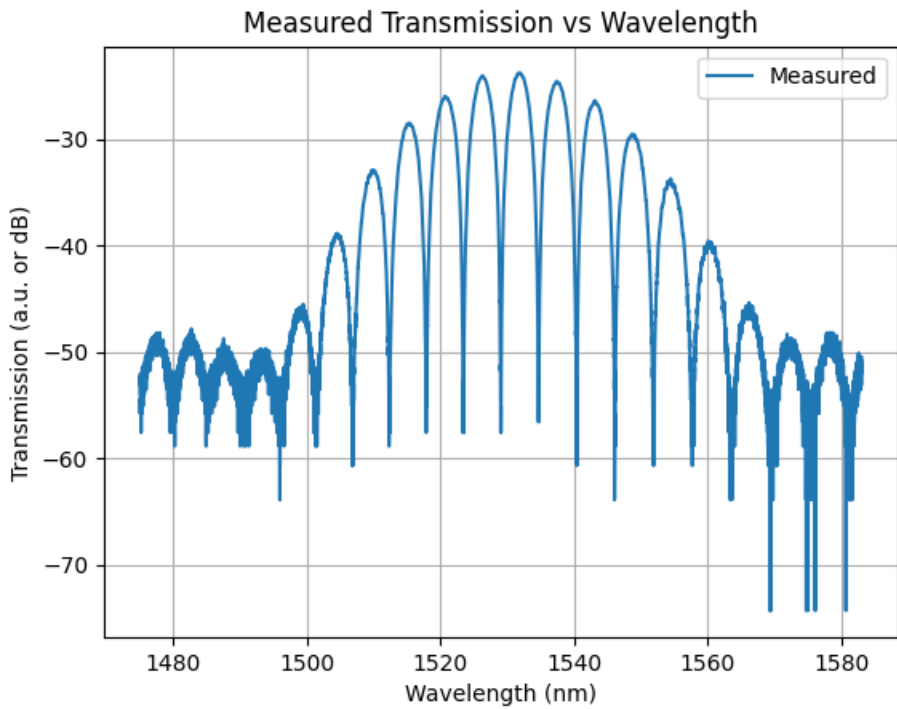


Figure 28: Raw measured transmission spectrum (example shown for MZIBDC2).

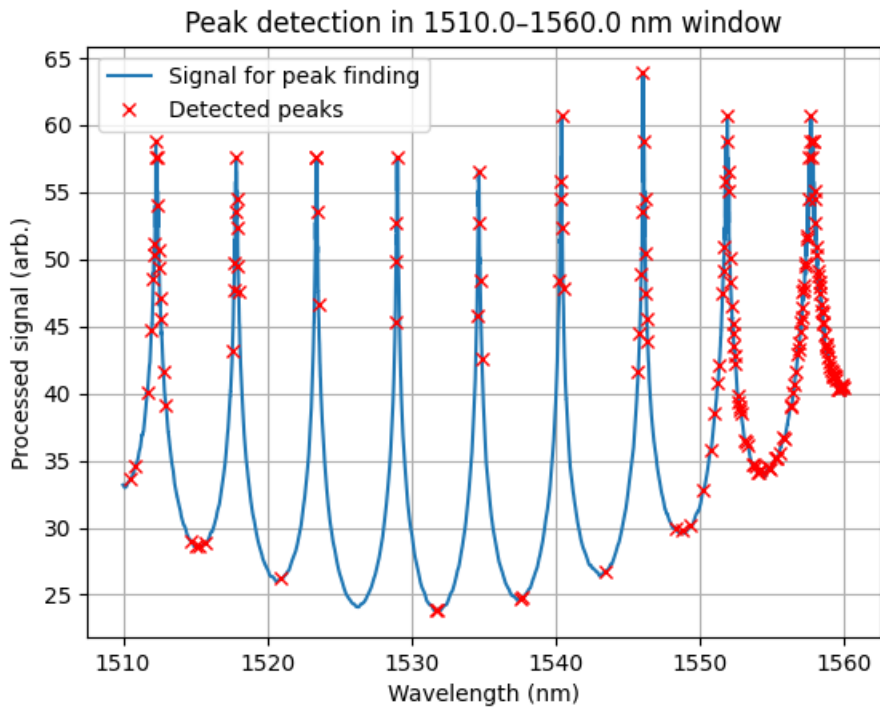


Figure 29: Initial peak detection on raw data. Noise produces many false peaks.

Savitzky–Golay Smoothing and Peak Filtering

To extract reliable peaks, a multi-step processing pipeline was implemented:

1. Savitzky–Golay smoothing to suppress high-frequency noise while preserving fringe envelopes.
2. Derivative-based peak detection on the smoothed curve.
3. Peak filtering based on prominence and minimum spacing to remove spurious detections.

The effect of smoothing is shown in Fig. 30. The cleaned peak detection used for FSR extraction is shown in Fig. 31.

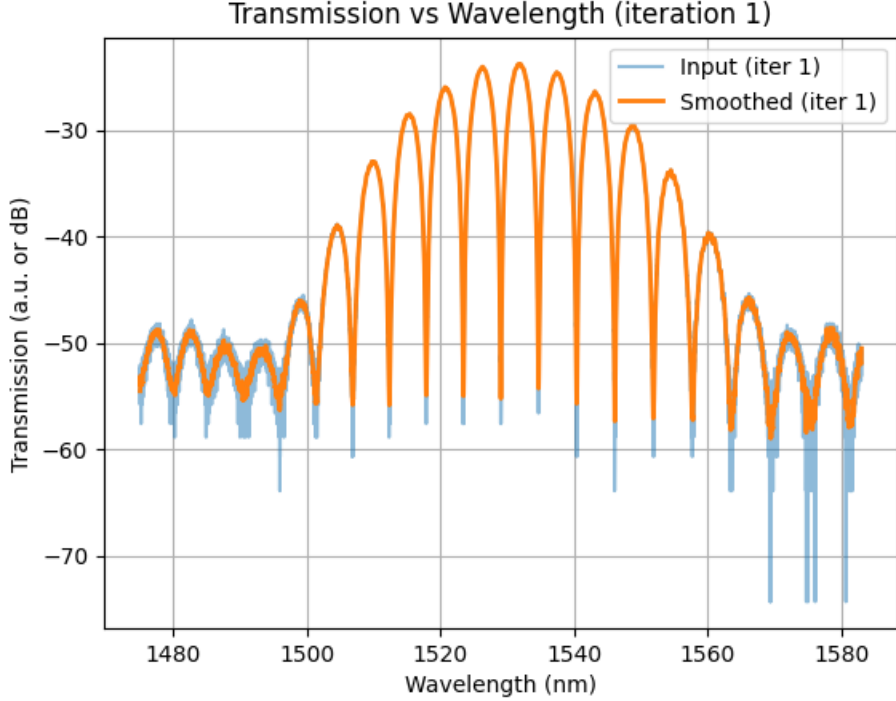


Figure 30: Smoothed transmission spectrum after Savitzky–Golay filtering (example: MZ-IBDC2).

Simulated and Measured FSR and Group Index

The interferometric peaks extracted above were used to compute the measured free-spectral range,

$$\text{FSR} = \lambda_{k+1} - \lambda_k,$$

and the corresponding group index,

$$n_g = \frac{\lambda_0^2}{\text{FSR } \Delta L}, \quad \lambda_0 \approx 1550 \text{ nm.}$$

Simulated values were obtained from the compact waveguide model fitted using MODE.

Discussion

The following key observations emerge:

- **MZIYY1_1** shows strong agreement between simulated and measured FSR, confirming the accuracy of both the compact model and fabrication.

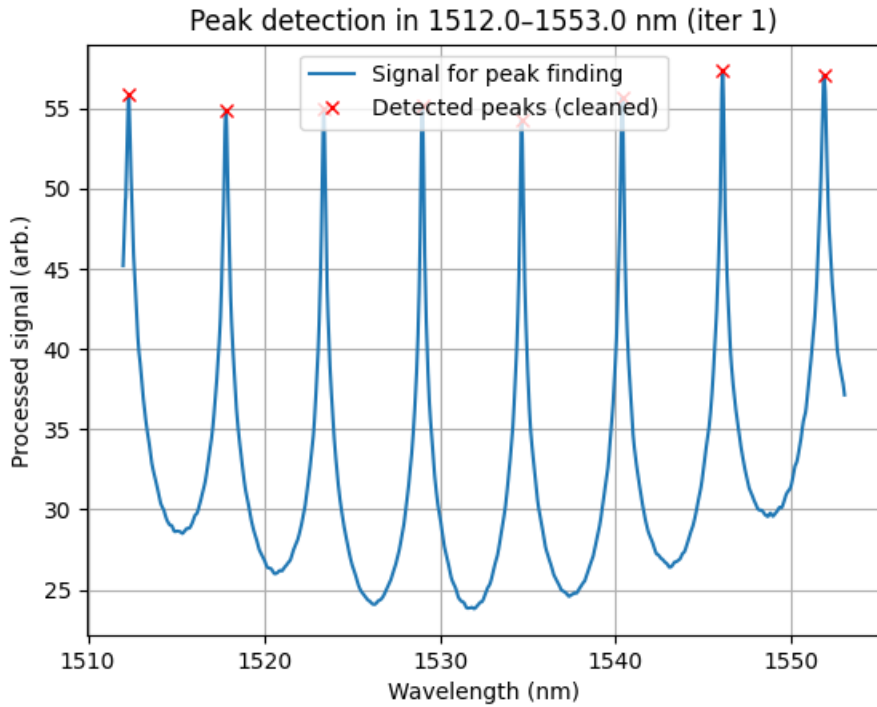


Figure 31: Cleaned peak detection after smoothing and peak filtering. Only true interference peaks remain.

Device	ΔL (μm)	FSR _{sim} (nm)	n_g,sim	FSR _{meas} (nm)	n_g,meas
MZIYY1_1	40.000	13.9622	4.30181	14.1360	4.24890
MZIBDC1	39.883	13.4648	4.47349	14.3920	4.18557
MZIBDC2	100.032	5.7679	4.16396	5.7680	4.16389

Table 11: Simulated and measured FSR and group index for Set-1 MZIs.

- **MZIBDC1** exhibits a noticeably larger measured FSR and thus a lower group index, likely due to increased sensitivity of broadband directional couplers to fabrication-induced phase imbalance.
- **MZIBDC2** shows nearly perfect agreement between experiment and simulation, validating the robustness of the compact waveguide model for larger path-length differences.

Notes on Data Processing Robustness

It should be emphasized that the smoothing and peak-filtering parameters **are not fixed universal values**. Instead, for each device:

- smoothing-window length,
- filter polynomial order,
- peak prominence threshold, and
- minimum peak spacing

were adjusted iteratively to ensure that only true interference peaks were retained.

Noise levels, ripple magnitudes, and signal distortions vary between devices, making a single fixed set of parameters unreliable. The final peak set used for FSR extraction was obtained only after verifying that all detected peaks were physically consistent and free of noise-induced artifacts.

11 Connecting Corner Analysis, Simulations, and Measurements

The simulated MZI responses in previous sections of the report were obtained using the nominal compact model for the TE mode, with $n_g \approx 4.20$ at 1550 nm.¹ The corner analysis above shows that realistic process variations in waveguide thickness and width naturally lead to n_g values between about 4.16 and 4.24 for the TE mode. This spread is directly reflected in the measured MZI data.

For the **Set-2 MZIs** (MZIYY20–MZIYY23), the measured group indices extracted from the de-embedded spectra (Table 8) fall in the range

$$n_{g,\text{meas}}^{\text{Set2}} \approx 4.18--4.25,$$

which lies entirely inside the TE corner band from Table 7. In particular:

- Devices with slightly *higher* measured n_g (MZIYY22, MZIYY23) are consistent with corners where the waveguide is a bit thicker and/or narrower (e.g., C4_tw_tmx-wmn), which increases optical confinement and group index.
- Devices closer to the *lower* end of the measured n_g band (MZIYY20) align with corners like C2_tw_tmnm-wmx, which combine a slightly thinner or wider waveguide.

This agreement gives strong evidence that:

1. the polynomial compact model extracted from MODE is accurate, and
2. the fabricated devices are well described by moderate deviations inside the assumed process window (\pm a few nm in thickness and width).

For the **Set-1 MZIs** (MZIYY1_1, MZIBDC1, MZIBDC2), the comparison in Table 9 shows:

- MZIYY1_1 and MZIBDC2 exhibit excellent agreement between simulated and measured FSR, indicating that their effective n_g is very close to the nominal compact-model value.
- MZIBDC1 shows a larger discrepancy: the measured FSR is higher and the extracted n_g is correspondingly smaller. This is most likely due to directional-coupler sensitivity (small phase and splitting-ratio shifts) rather than a gross change in the straight waveguide index itself. Nevertheless, the measured n_g still lies within the extended TE corner band when uncertainties in ΔL are taken into account.

Overall, the measurements confirm the main trends predicted by simulation:

- Larger path-length differences lead to smaller FSR (Set 1 vs. Set 2).
- Bend layouts in Set 2 do not introduce measurable additional loss or dispersion at the chosen bend radius; differences between MZIYY20–23 are dominated by straight-waveguide process variation.
- The spread in measured n_g is consistent with the TE corner analysis ranges, providing a quantitative link between the compact waveguide model and fabricated devices.

¹Values summarized in Tables 3 and 4 of the original report.:contentReference[oaicite:1]index=1

12 Conclusions and Remarks

The complete workflow followed in this project—from layout design in KLayout, through MODE-based compact-model extraction and INTERCONNECT simulations, to post-processed measurements of seven MZI devices and four waveguides—has provided a coherent picture of how design choices and fabrication variations manifest in silicon photonic circuits.

Key conclusions are:

1. **Waveguide behaviour:** The TE-mode compact model at 1550 nm yields $n_g \approx 4.20$ for the nominal geometry. Corner analysis shows that realistic thickness/width variations move n_g within roughly 4.16–4.24 (TE), and 3.48–3.82 (TM). Measured MZI group indices are fully consistent with this TE band, indicating that the process variations on the fabricated wafer are within the assumed windows.
2. **Waveguide loss:** The cut-back style measurement using short waveguides (200–800 μm) shows only about 0.6 dB spread between structures, dominated by grating-coupler differences rather than true propagation loss. This suggests that the intrinsic waveguide loss is relatively low (a few dB/cm), but longer test structures (several cm) would be needed for a precise extraction.
3. **MZI Set 2 (bend study):** Both simulations and de-embedded measurements of MZIYY20–MZIYY23 show nearly identical FSR and fringe shape, confirming that the chosen bends (radius 5 μm with Bézier optimization) introduce negligible additional loss or dispersion. Device-to-device differences are explained by small shifts in n_g captured by the corner analysis.
4. **MZI Set 1 (coupler and ΔL study):** The three devices highlight how path-length difference and combiner choice affect the spectral response. The Y-combiner and one of the BDC-based MZIs (MZIBDC2) closely match the compact-model predictions, while MZIBDC1 shows increased sensitivity, illustrating that directional couplers can amplify small fabrication-induced asymmetries.
5. **Robust data processing:** Reliable FSR extraction required careful Savitzky–Golay smoothing and iterative peak filtering. There is no single “magic” set of parameters; instead, the algorithm was tuned per device to suppress false peaks while preserving the physical interference pattern.

Taken together, these results show that the compact waveguide models obtained from MODE, combined with a simple corner analysis, can accurately predict the behaviour of fabricated MZI circuits within realistic process windows. The agreement between simulated and measured FSR and group index across seven MZIs is particularly encouraging for future circuit-level designs using the same PDK.

Acknowledgments

This work was carried out as part of the *Silicon Photonics Design, Fabrication, and Data Analysis* course offered on edX by the University of British Columbia (UBC). I would like to express my sincere gratitude to the course instructor, **Prof. Lukas Chrostowski**, for his exceptional teaching, structured guidance, and the clarity with which he presented complex concepts in silicon photonics. As someone who was almost an entrant into this field, I found his course remarkably well designed and accessible; it enabled me to grasp and appreciate a great deal of the subject matter, far more than I initially expected. I truly cannot thank him enough for this learning experience.

I am also deeply thankful to the teaching assistant, **Mateo Castel**, for his continuous support, timely feedback, and insightful discussions throughout the course. His assistance was invaluable in understanding the workflows and in debugging various issues throughout the course.

Additionally, I extend my appreciation to the entire UBC Silicon Photonics teaching team and the broader course community on edX. The interactive forums, shared examples, and collaborative problem discussions greatly enhanced the learning experience. Their collective efforts made the course not only intensive but also highly enjoyable and rewarding.

Finally, I acknowledge the developers and contributors of the open-source tool *KLayout* and the supporting Ansys Lumerical documentation, both of which were essential in completing the layout, waveguide analysis, and compact modelling work presented in this report.

References

1. L. Chrostowski and M. Hochberg, *Silicon Photonics Design, Fabrication and Data Analysis* (University of British Columbia), edX Online Course, 2023. Available: <https://www.edx.org/>.
2. L. Chrostowski and M. Hochberg, *Silicon Photonics Design: From Devices to Systems*. Cambridge University Press, 2015.
3. G. T. Reed and A. P. Knights, *Silicon Photonics: An Introduction*. Wiley, 2004.
4. Ansys Lumerical, *Mode Solutions, DEVICE, and INTERCONNECT Documentation and Application Examples*. Available: <https://optics.ansys.com/>.
5. Ansys Lumerical, *Silicon Photonics Learning Resources*. Available: <https://optics.ansys.com/hc/en-us/categories/360002881213-Learning>.
6. Silicon Photonics Tutorials and Lectures, YouTube educational channels (various instructors), covering silicon waveguides, MZI circuits, compact modelling, and Lumerical simulation workflows.